frequency–voltage conversion is made in a secondary low-frequency PLL such that the phase detector output of the microwave PLL gives, in a logic level format, an indication of the lock condition in the main PLL.

This circuit has been used with success in microwave PLO's in which the phase detection was made at 290 MHz, 2.55 GHz, 27 GHz, and 29.7 GHz.

References

[1] F. M. Gardner, *Phaselock Techniques*. New York: Wiley, 1979

[2] W. P. Robins, *Phase Noise in Signal Sources* (IEE Telecommunications Series 9). London: Peter Peregrinus Ltd., 1982

[3] A. B. Carlson, *Communication Systems*. New York: McGraw-Hill, 1975

[4] L. E. Franks, *Signal Theory*. Englewood Cliffs, NJ: Prentice Hall, 1975

[5] J. Berenguer, J. Bara, and A. Comeron, "Compact and simple ×3 (9 to 27 GHz) PLL frequency multiplier using harmonic phase detection," in *Proc. 41st Ann. Symp. Frequency Control* (Philadelphia), May 1987, pp. 492–494.

Polarization Effects on Microwave Imaging of Dielectric Cylinder

TAH-HSIUNG CHU, MEMBER, IEEE

Abstract—**In this paper, theoretical and experimental studies of frequency-swept microwave imaging of an infinitely long lossless homogeneous dielectric cylinder illuminated by a right-hand circularly polarized (RHCP) plane wave are presented. The reconstructed polarization-dependent microwave image can be seen as embodying contributions from specular, axial, glory, and stationary ray components of the scattered field of the selected receiving polarization state. An automated microwave imaging system employing frequency and polarization diversity techniques is utilized to verify the theoretical and numerical results.**

I. Introduction

Frequency-swept microwave imaging of dielectric objects satisfying the Born approximation has been shown to be a cost-effective tool in nondestructive evaluation [1]. The polarization effect on the reconstructed microwave image is negligible when the dielectric object is weakly scattering. However, as the product of object radius in wavelength and the change in object refraction index from its surrounding medium becomes greater than 0.175, the Born approximation fails [2]; hence the polarization states of the illuminating and receiving fields must be taken into consideration. In this paper, theoretical and experimental studies of the polarization effects on the frequency-swept microwave image of an infinitely long dielectric cylinder not satisfying the Born approximation are presented.

II. Theoretical Considerations

Consider an infinitely long homogeneous nondispersive dielectric cylinder with relative dielectric constant ϵ_r and radius a in a backscattering arrangement as shown in Fig. 1 being illuminated by a right-hand circularly polarized (RHCP) plane wave $\vec{E}_R^i$ expressed as

$$\vec{E}_R^i = \frac{1}{\sqrt{2}}\left(E_\phi^i\hat{\phi} - jE_z^i\hat{z}\right) = \frac{1}{\sqrt{2}}E_0 e^{-jkR}\left(\hat{\phi} - j\hat{z}\right) \qquad (1)$$

Manuscript received January 25, 1988; revised April 28, 1988.

The author is with the Department of Electrical Engineering, National Taiwan University, Taipei, Taiwan, R.O.C.

IEEE Log Number 8822155

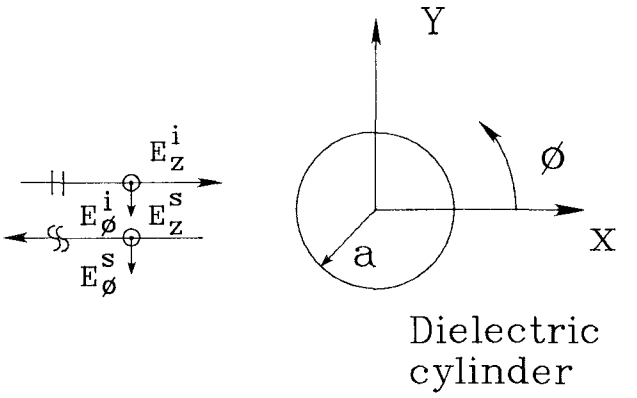

Fig. 1 The scattering geometry

where $\exp(j\omega t)$ is implied. In the following, linearly polarized scattered field components and their reconstructed images will be discussed first. Results are then extended to the circular polarization case.

The scattered far fields for each linear polarization state in the resonance and high-frequency regions ($ka > 1$) can be characterized by rays using a modified geometrical optics method [3]–[5], and they are given as

$$E_\phi^s = E_0\sqrt{\frac{a}{2R}}\,e^{jkR} \cdot\left[f_0 e^{j\theta_0} + \sum_l f_{Al}e^{j\theta_{Al}} + \sum_m f_{Gm}e^{j\theta_{Gm}} + \sum_n f_{Sn}e^{jQ_{sn}}\right] \qquad (2)$$

and

$$E_z^s = E_0\sqrt{\frac{a}{2R}}\,e^{jkR} \cdot\left[g_0 e^{j\psi_0} + \sum_l g_{Al}e^{j\psi_{Al}} + \sum_m g_{Gm}e^{j\psi_{Gm}} + \sum_n g_{Sn}e^{j\psi_{Sn}}\right]. \qquad (3)$$

Equations (2) and (3) show that the backscattered fields for each linear polarization state are superpositions of various ray components. The first term is the specular ray. The terms with subscripts A, G, and S are axial, glory, and stationary rays and l, m, and n are numbers of internal reflection for each ray component inside the dielectric cylinder as described in [3]–[5]. For example, f_{A1} and θ_{A1} are the amplitude and phase of the single bounce axial ray component in the E_ϕ^s field. The various ray amplitudes are related to the cylinder radius, dielectric constant, and radius of curvature of the emerging ray phase front after interaction with the cylinder surface, and the ray phases are equal to the product of the wavenumber k and the optical length of a given ray between entrance and emergence. They are polarization dependent and are given in [4] and [5].

Since the phase term for each ray component is linearly proportional to the optical length it travels, one-dimensional Fourier inversion of the scattered far field acquired using the frequency diversity technique (i.e., varying the wavenumber k) gives a range profile of the illuminated cylinder for each selected

polarization state as

$$E_0\sqrt{\frac{a}{2R}}\left[f_0\delta(R-r_0)+\sum_l f_{Al}\delta(R-r_{Al})+\sum_m f_{Gm}\delta(R-r_{Gm})+\sum_n f_{Sn}\delta(R-r_{Sn})\right] \quad (4)$$

and

$$E_0\sqrt{\frac{a}{2R}}\left[g_0\delta(R-s_0)+\sum_l g_{Al}\delta(R-s_{Al})+\sum_m g_{Gm}\delta(R-s_{Gm})+\sum_n g_n\delta(R-s_{Sn})\right] \quad (5)$$

where the spikes in the profile represent the contribution of each ray component.

Due to the reversal of the sense of circular polarization upon reflection, the scattered fields expressed in terms of circular polarization are given as

$$\vec{E}_R^s=\frac{1}{\sqrt{2}}\left[E_\phi^s\hat{\phi}+jE_z^s\hat{z}\right] \quad (6)$$

and

$$\vec{E}_L^s=\frac{1}{\sqrt{2}}\left[E_\phi^s\hat{\phi}-jE_z^s\hat{z}\right]. \quad (7)$$

By substituting (2) and (3) into (6) and (7), the RHCP and LHCP scattered fields can be shown to be

$$E_R^s=E_0\sqrt{\frac{a}{2R}}\,e^{jkR}\left[\sum_{l=5}\left(f_{Al}e^{j\theta_{Al}}+g_{Al}e^{j\Psi_{Al}}\right)+\sum_m\left(f_{Gm}e^{j\theta_{Gm}}+g_{Gm}e^{j\psi_{Gm}}\right)+\sum_n\left(f_{Sn}e^{j\theta_{Sn}}+g_{Sn}e^{j\psi_{Sn}}\right)\right] \quad (8)$$

and

$$E_L^s=E_0\sqrt{\frac{a}{2R}}\,e^{jkR}\left[\left(f_0e^{j\theta_0}-g_0e^{j\psi_0}\right)+\sum_l\left(f_{Al}e^{j\theta_{Al}}-g_{Al}e^{j\psi_{Al}}\right)+\sum_m\left(f_{Gm}e^{j\theta_{Gm}}-g_{Gm}e^{j\psi_{Gm}}\right)+\sum_n\left(f_{Sn}e^{j\theta_{Sn}}-g_{Sn}e^{j\psi_{Sn}}\right)\right]. \quad (9)$$

Since the amplitude terms are $f_0=-g_0$, $f_{A1}=-g_{A1}$, and $f_{A3}=-g_{A3}$ and the phase terms are $\theta_0=\psi_0$, $\theta_{A1}=\Psi_{A1}$, and $\theta_{A3}=\psi_{A3}$ [4], the specular, single, and third bounce axial rays disappear in (8). Therefore, the significant ray components in the RHCP scattered field are single bounce glory and stationary rays. The specular, single bounce axial, glory, and stationary rays are the significant ray components in the LHCP scattered field. The range profiles obtained from one-dimensional Fourier inversion of (8) and (9) will then consist of spikes contributed from these significant rays. The absolute value of the RHCP and LHCP range profiles are defined as the RHCP and LHCP dielectric images in this paper. This is based on the observation that an image is formed by reflection from interface or discontinuities.

By rotating the dielectric cylinder in the ϕ direction, two-dimensional RHCP and LHCP scattered fields can be accessed using the frequency diversity technique and presented in a polar format [1]. The radial distance for each line represents the frequency used, and the polar angle equals the rotation angle ϕ. The RHCP and LHCP microwave images of the test cylinder are then reconstructed using two-dimensional Fourier inversion.

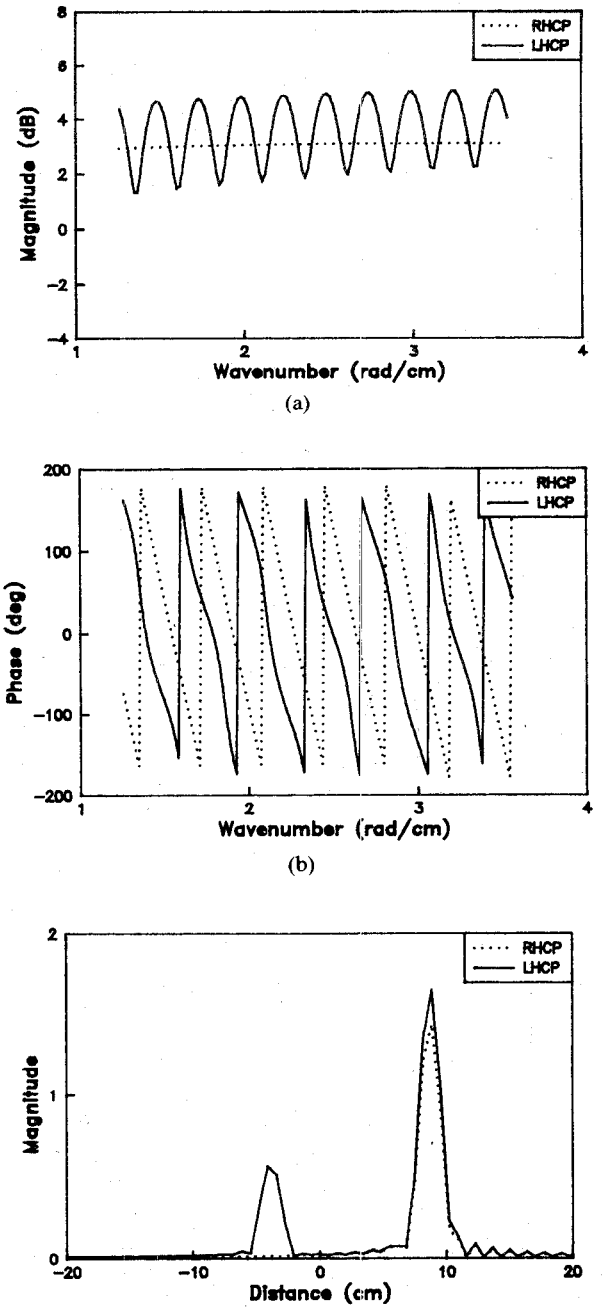

Fig. 2. One-dimensional simulation results of (a) magnitude and (b) phase of RHCP and LHCP scattered fields and (c) reconstructed images using modified geometrical optics approach.

In the next section, numerical and experimental results of RHCP and LHCP dielectric images of a circular cylinder ($a=3.8$ cm, $\epsilon_r=2.56$) under RHCP plane wave illumination will be presented.

III. Numerical and Experimental Results

Fig. 2(a) and (b) gives the magnitude and phase of RHCP and LHCP scattered fields calculated based on the modified geometrical optics method. The frequency range used is 6–17 GHz or the wavenumber k varies from 1.26 to 3.56 rad/cm. The range for ka is then 4.79–13.5 rad, i.e., in the high-frequency region. The reconstructed one-dimensional polarization-dependent di-

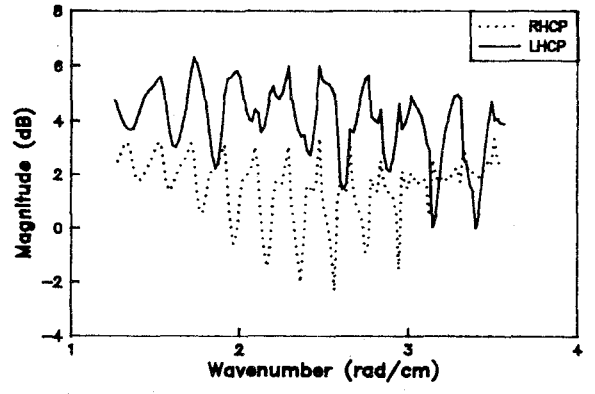

(a)

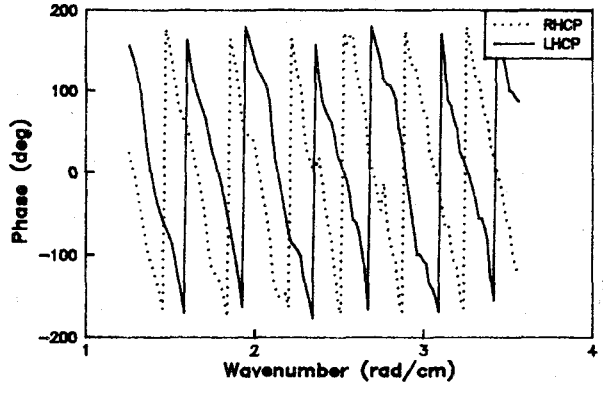

(b)

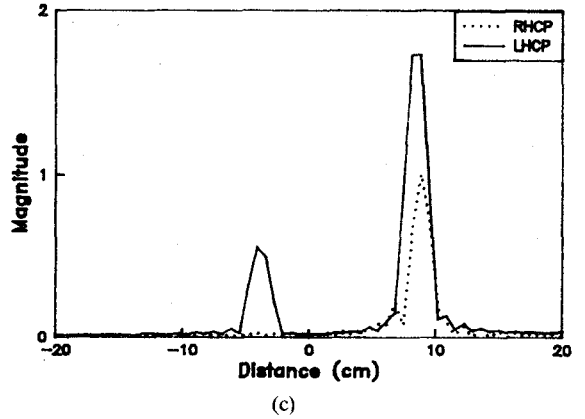

(c)

Fig. 3. One-dimensional simulation results of (a) magnitude and (b) phase of RHCP and LHCP scattered fields and (c) reconstructed images using boundary value solution approach.

electric images are shown in Fig. 2(c). The LHCP image contains two spikes, in which the first spike is due to the specular reflection occurring at 3.8 cm, and the second one at about -6.3 cm is contributed from the single bounce axial, glory, and stationary rays. The contribution of higher order terms is not appreciable and hence is not shown. The RHCP image shows only one spike contributed from the single bounce glory and stationary rays, as discussed in Section II. The spike location in the RHCP image is in about the same position as the second spike in the LHCP image. These polarization-dependent dielectric images are very close to those calculated from the boundary value solution of the scattered fields as shown in Fig. 3 for comparison.

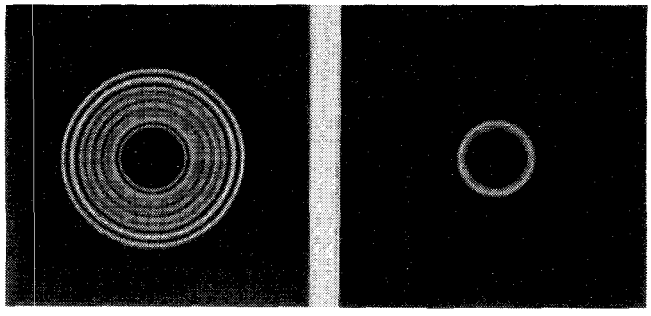

(a)

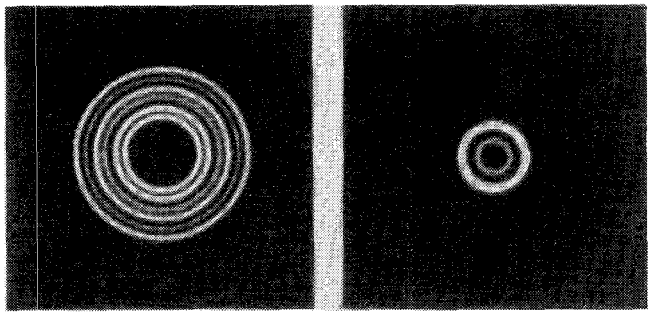

(b)

Fig. 4. Two-dimensional simulation results of (a) RHCP and (b) LHCP scattered fields (left side) and reconstructed images (right side) using modified geometrical optics approach.

Shown in Fig. 4(a) are the calculated RHCP and LHCP scattered fields presented in polar format consisting of 200 radial lines equally spaced over 360°, with each line containing 64 equally spaced points covering 6–17 GHz. The reconstructed RHCP and LHCP images from two-dimensional Fourier inversion are shown in Fig. 4(b). The LHCP image contains two concentric circles. The inner one due to the specular reflection gives the size of the test cylinder. The outer one is due to the contribution of the single bounce axial, glory, and stationary rays. The RHCP image gives one circle about the same size as the outer circle in the LHCP image.

In the experiment, a Plexiglas cylinder ($\epsilon_r = 2.56$) with length 120 cm and radius 3.8 cm is mounted on a computer-controlled positioner and illuminated by a RHCP plane wave. The entire automated measurement sequence consists of angular positioning of the cylinder in increments of 1.8° over 360°, incremental frequency tuning over 6–17 GHz, recording the amplitude and phase from the coherent receiver, and polarization selection of the receiving antenna. Shown in Fig. 5 are the measured RHCP and LHCP scattered fields and the reconstructed images. They are shown to be in good agreement with the simulation results.

IV. Discussion

Analytical and experimental studies of the polarization-dependent frequency-swept microwave images of a lossless dielectric cylinder not satisfying the Born approximation and illuminated with a RHCP plane wave are presented. The LHCP and RHCP dielectric images of the scattering cylinder are shown to be different. Only the LHCP image has detail that corresponds to the specular reflection from the cylinder interface and gives the size of the test cylinder. The remaining detail is due to the multiple scattering within the cylinder, which is represented by a larger and stronger circle due to the contribution of the single

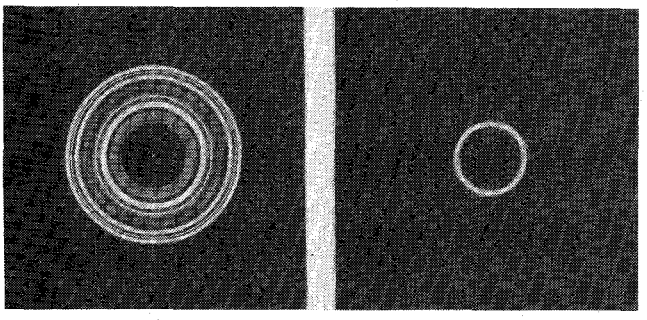

(a)

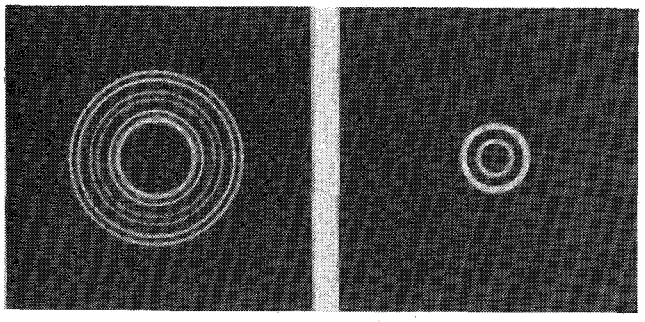

(b)

Fig. 5. Experimental results of (a) RHCP and (b) LHCP scattered fields (left side) and reconstructed images (right side).

bounce axial, glory, and stationary rays. The RHCP image gives only one circle, due to the single bounce glory and stationary rays.

The results presented here lead to a better understanding of the role of polarization in microwave imaging for conveying more information about a dielectric object which does not satisfy the Born approximation. The method presented also illustrates the usefulness of microwave imaging systems using frequency and polarization diversity techniques in understanding the back-scattering mechanism of the test dielectric object. The polarization effects have also been observed in the microwave images of a biological object in the forward scattering arrangement [6].

REFERENCES

[1] T. H. Chu and N. H. Farhat, "Frequency-swept microwave imaging of dielectric objects," *IEEE Trans. Microwave Theory Tech.*, vol. MTT-36, pp. 489–493, Mar. 1988.

[2] M. Slaney, A. C. Kak, and L. Larsen, "Limitations of imaging with first-order diffraction tomography," *IEEE Trans. Microwave Theory Tech.*, vol. MTT-32, pp. 860–874, Aug. 1984.

[3] R. G. Kouyoumjian, L. Peters, Jr., and D. T. Thomas, "A modified geometrical optics method for scattering by dielectric bodies," *IEEE Trans. Antennas Propagat.*, vol. AP-11, pp. 690–703, Nov. 1963.

[4] W. C. Y. Lee, L. Peters, Jr., and C. H. Walter, "Electromagnetic scattering by gyrotropic cylinders with axial magnetic fields," The Electro Science Lab., The Ohio State University, Columbus, OH, Rep. 1116-48, May 1964.

[5] D. E. Barrick, "A note on scattering from dielectric bodies by the modified geometrical optics method," *IEEE Trans. Antennas Propagat.*, vol. AP-16, pp. 275–277, Mar. 1968.

[6] L. E. Larsen and J. H. Jacobi, "The use of orthogonal polarizations in microwave imagery of isolated canine kidney," *IEEE Trans. Nucl. Sci.*, vol. NS-27, pp. 1184–1190, June 1980.